An Adaptive Reclosing Scheme Based on Phase Characteristics for MMC-HVDC Systems

Tao Zheng, *Member, IEEE*, Wenxuan Lv, and Rui Li, *Member IEEE*

***Abstract*—To improve the reliability of power supply, reclosing schemes are required after transient faults, which commonly occur in overhead line based high voltage DC (HVDC) systems. However, in the event of permanent faults, the auto-reclosing scheme may cause a severe strike. To avoid the severe impacts caused by permanent faults, the fault type should be discriminated before activating the reclosing scheme. Therefore, an adaptive reclosing scheme based on phase characteristics is proposed in this paper. Firstly, the modulation of a periodic voltage by actively controlling the hybrid DC circuit breaker (DCCB) is introduced. Then, a cascaded π equivalent model and its decoupling algorithm are presented to analyze the frequency-domain characteristics of the measured impedance of the coupled overhead lines. From the frequency-domain characteristics, the frequency of the periodic detecting voltage is determined to analyze the phase features of the measured impedance at primary frequency. The permanent or transient faults can thus be accurately identified by using these different phase characteristics, with negligible influence on the healthy lines. In addition, the proposed scheme is robust to various fault resistances, leading to improved reliability. The effectiveness of the proposed scheme is verified in PSCAD/EMTDC.**

***Index Terms*— adaptive reclosing scheme, coupled cascaded π model, phase characteristics, MMC-HVDC, fault resistance**

I. Introduction

With the rapid development of renewable energy, flexible DC transmission system has become a hot research topic because of its flexible control and low transmission power losses. Due to the increased demand for large-capacity transmission over long distances [1], the modular multilevel converter-based high voltage direct current (MMC-HVDC) transmission system is required to optimize energy resources and reduce costs. In such a situation, the overhead lines (OHLs) are more suitable than cables. For example, the ±500 kV MMC-HVDC transmission project with OHLs has been in operation at Zhangbei, China [2]. However, since the OHLs operate in the outdoor environment, pole-to-ground faults are common and most of them are transient. Therefore, the reclosing scheme is crucial to ensure the reliability and availability of the power system. The auto-reclosing scheme has been widely used in AC systems, but it may face challenges in DC systems due to the fast-rising rate and high amplitude of the fault current. A failed auto-reclose in the event of permanent faults will cause a severe secondary impact on the whole system and endanger the safe and stable operation of the converters [3]. Therefore, it is essential to distinguish the type of faults before reclosing and how to avoid reclosing on permanent faults is one of the problems to be solved urgently. In this situation, adaptive reclosing schemes deserve further study in the HVDC system [4][5].

So far, a number of adaptive reclosing schemes have been proposed for the HVDC system [6]–[17]. According to whether the control is based on converters or direct current circuit breakers (DCCBs), these schemes are divided into two categories.

- **Converter-based schemes:** The converter-based adaptive reclosing schemes actively control the converters (e.g., full-bridge modular multilevel converter (FB-MMC)) to identify the fault types. In [6], the nonlinear interdependence between the fault resistance and the current is used to detect transient faults. However, this method only applies to FB-MMC HVDC and works improperly under high resistance faults. In [7] and [8], a fault identification method based on active pulse injection from hybrid MMC is proposed. By measuring the refracted voltage, fault characteristics can be identified. However, both schemes in [7] and [8] need a high sampling rate to capture the traveling wave and affect the normal operation of the healthy parts of the DC network.
- **DCCB based schemes:** In these schemes, the fault types are identified based on the hybrid DCCB. The schemes are classified into three groups by the identification methods:
  1) Group 1 [9], [10]. Reference [9] proposes an auto-reclosing scheme by closing sub-modules of DCCB sequentially. In [10], A soft reclosing model for the hybrid DCCBs is proposed by inserting an additional resistance into the DC system. This group decreases the secondary strike when reclosing on permanent faults, but it can not identify the fault type before reclosing, and the impact of a failure reclosure still exists.
  2) Group 2 [11], [12], [13] uses the line voltage of DCCB to identify the fault types. The line voltage will hold zero when the fault is permanent; otherwise, the voltage will rise. This criterion is simple, but the threshold of the line voltage needs to be set, and the identification needs time delay to avoid the influence of oscillation. This method is first proposed in [13]. Reference [11] uses the integration of line

This work is supported by the Joint Funds of the National Natural Science Foundation of China (Grant No. U216620017), and by the State Key Laboratory of Alternate Electrical Power System with Renewable Energy Sources (Grant No. LAPS21011).

T. Zheng, W. Lv are with the State Key Laboratory of Alternative Electrical Power System with Renewable Energy Sources, North China Electric Power University, Beijing 102206, China (e-mail: zhengtao_sf@126.com).

R. Li is with the Department of Electronic and Electrical Engineering, University of Strathclyde, Glasgow, G1 1XW UK (e-mail:rui.li@strath.ac.uk).

voltage to avoid the impact of oscillation, but the integration time is hard to select. Reference [12] mainly focuses on the discrimination of pole-to-ground faults and pole to dedicated metallic return fault.

3) Group 3 [14], [15], [16], [17] are based on the characteristics of the traveling wave to identify the fault type. The detecting pulse is generated by hybrid DCCB in [14], [15], [16], while by the fault energy absorption module in [17] to avoid the impact of the current limiting reactor. This group of methods needs high sampling frequency to capture the traveling wave and minimize the dead zone. Besides, the traveling wave is sensitive to fault resistance.

The cascaded full bridge DCCBs (CFB-DCCBs), used in the Zhoushan 5-terminal HVDC project in China [18], have multi-branches and flexible controllability and are thus considered in this paper. The main contributions of this paper are:

- Considering the problems Group 3 faced, the proposed adaptive reclosing scheme utilizes the phase characteristics of measured impedance to distinguish fault types. The detecting voltage is preset offline through calculation so that the criterion is simple and reliable with low sampling frequency. Besides, the proposed scheme is adaptable to high fault resistance, leading to improved reliability.
- Comparing with Group 1 and 2, the proposed scheme can accurately identify permanent faults before reclosing without affecting the non-fault lines and is robust to oscillations.

The rest of the paper is structured as follows. Section II introduces the fault detecting voltage modulation at a certain frequency by switching the full-bridge sub-module (FBSM) of the transfer branch. In Section III, the coupling characteristics of the cascaded π equivalent circuit for OHLs and the decoupling methods are introduced to analyze faults' frequency-domain characteristics. Then the adaptive reclosing scheme and the criteria for the fault differentiation are presented in Section IV. In Section V, simulation results in PSCAD / EMTDC environment verify the feasibility of the proposed scheme. Finally, Section VI concludes the paper.

II. Modulation of Detecting Voltage

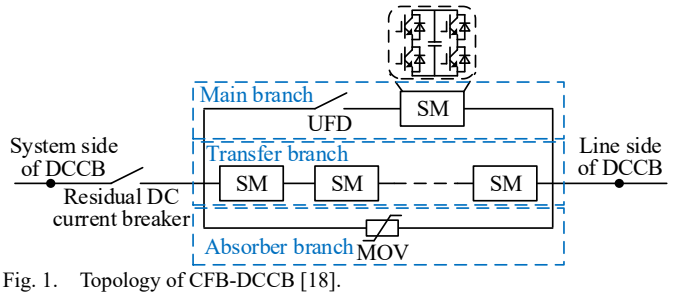

Fig. 1. Topology of CFB-DCCB [18].

To highlight the phase characteristics of different faults, a periodical detecting voltage is required, which can be generated by controlling the transfer branch of a CFB-DCCB, as shown in Fig. 1 [18]. The CFB-DCCB is made up of three parallel paths, where the main branch consists of a lower number of full-bridge sub-modules (FBSM) and an ultrafast disconnector (UFD). During normal operation, load current mainly flows through the main branch. The second path is the transfer branch and is made up of series cascaded FBSMs. Fault current could be reduced by blocking FBSMs after fault occurrence. The last path is the absorber branch and is composed of metal oxide varistor (MOV). The energy stored in DC lines needs to be dissipated by the MOV for fault isolation [19].

The fault clearing process of CFB-DCCB can be divided into four states: normal operation state, fault current transfer state, fault current breaking state, and energy release state [20]. After the fourth state, the fault current attenuates to zero and thus, the breaking process of the circuit breaker ends. The reclosing operation is carried out after 200 ms for deionization to ensure that the DC line's insulation level and DCCB's current interruption capability are fully recovered [19] [21].

After isolation of the faulty line, the voltage of the transfer branch will be equal to the DC system voltage [18]. If the RCB remains closed, the converter and the DC faulty line are still connected through the transfer branch, which provides a conduction path for the breaker to apply detecting voltage on the faulty line.

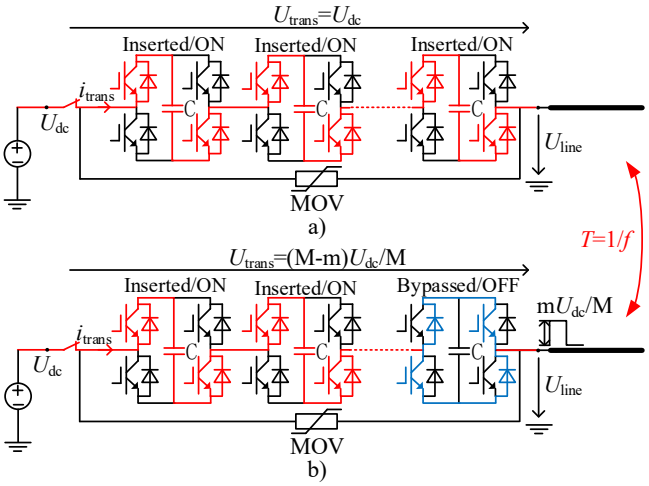

Fig. 2. Control strategy of transfer branch: (a) all FBSMs inserted and (b) *m* FBSMs bypassed

The system voltage U_{dc} is equal to the transfer branch voltage U_{trans} when the FBSMs of the transfer branch are all inserted, as illustrated in Fig. 2 (a). Thus the line to ground voltage U_{line} remains around zero. Assuming the total number of FBSMs in the transfer branch is M, if m FBSMs are bypassed as shown in Fig. 2 (b), U_{trans} will decrease to $(M\text{-}m)U_{dc}/M$, and the line voltage will become mU_{dc}/M. In this way, a step voltage of mU_{dc}/M is generated and applied at the faulty line. If this process is repeated at frequency f and the FBSM capacitor voltages are balanced during the switching process by proper balancing control [22], a square-wave detecting voltage can thus be obtained, as shown in Fig. 2. The duty cycle of the detecting voltage is selected as 50% to eliminate even harmonics and increase the primary frequency component [23]. The detecting voltage U_{line} is expressed as:

$$U_{line}=\begin{cases}\dfrac{m}{M}U_{dc} & 0\le t\le T/2\\ 0 & T/2\le t\le T\end{cases}. \tag{1}$$

To accurately extract the phase characteristics, the primary frequency component $\dot{U}_{\text{line1}}$ of the detecting voltage is obtained by fast Fourier decomposition:

$$\dot{U}_{\text{line1}}=\frac{2mU_{\text{dc}}}{M\pi}e^{j2\pi ft}=\frac{2mU_{\text{dc}}}{M\pi}\sin(2\pi ft). \quad (2)$$

The periodic switching of the FBSMs potentially poses a negative impact on the lifetime of the DCCB and to reduce such impact, the FBSMs are selected by an equalization algorithm. For example, if one FBSM is selected to modulate the detecting voltage in a switching cycle, it will not participate in the voltage modulation in the next cycles until all the SMs have been used equally. Besides, DCCBs at two sides of the line are used to generate detecting voltage alternatively, which further decreases the negative impact.

III. Frequency-Domain Characteristics of OHLs

A two-terminal bipolar HVDC transmission system as shown in Fig. 3 is considered to analyze the frequency-domain characteristics of OHLs when the detecting voltage is applied. The parameters of the system and DCCB are listed in Table I and II, respectively. Pole-to-ground DC faults are more common than pole-to-pole faults in HVDC systems and thus considered in this paper.

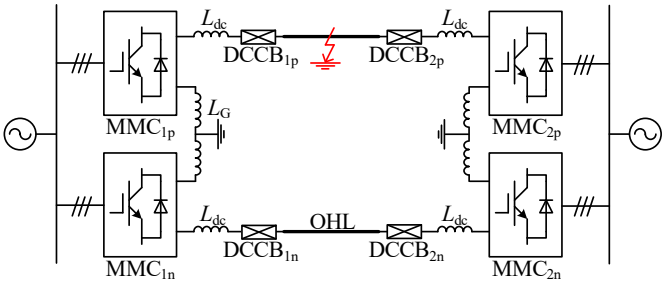

Fig. 3. Topology of tested bipolar HVDC system.

TABLE I
Parameters of System

Parameters	Value
DC voltage	±500 kV
AC voltage	220 kV
Rated power of converters	300 MW
Arm inductance L_{arm}	144 mH
SM capacitance C_{SM}	5 mF
SM number per arm N	200
DC line length	400 km
DC reactance L_{dc}	0.15 H
DC reactance L_G	0.3 H

TABLE II
Parameters of DCCB

Parameters		Value
Main branch	SM number	2
	Time delay of UFD	2 ms
Transfer branch	SM number	14
	Capacitance of SM	500 uF
Absorber branch	Rated voltage of MOV	750 kV
	Number of MOV in parallel	1
	Number of MOV in series	2
	DC breaking current	25 kA
	Residual DC breaking current	0.02 kA

A. Decoupling of cascaded π equivalent circuit of OHLs

Considering the distributed parameters of a long OHL, the cascaded π equivalent circuit is adopted in this paper as shown in Fig. 4. The resistance R, inductance L and capacitance C at different frequencies are calculated using frequency-dependent characteristics [24]. Coupling capacitance C_{m} and inductance L_{m} are added into each π equivalent circuit to represent the coupling phenomenon of OHLs.

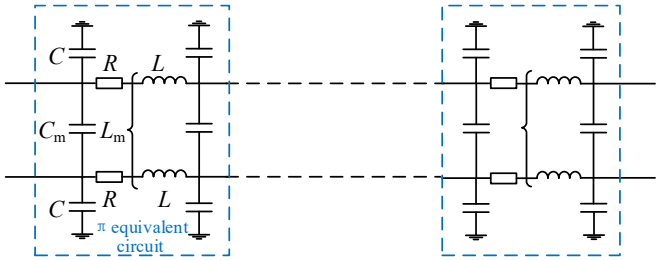

Fig. 4. Coupled cascaded π model of OHLs.

To simplify the analysis of the frequency-domain characteristics of the coupled π equivalent circuit, a phase-mode transformation matrix **p** is introduced to decouple the circuit, as expressed as:

$$\mathbf{p}=\begin{bmatrix}1 & 1\\ 1 & -1\end{bmatrix}. \quad (3)$$

With the phase-mode transformation, voltages (U_0, U_l) and currents (I_0, I_l) in zero-mode and line-mode can be described as:

$$\begin{bmatrix}U_0\\ U_l\end{bmatrix}=\mathbf{p}\begin{bmatrix}U_{\text{p}}\\ U_{\text{n}}\end{bmatrix},\quad \begin{bmatrix}I_0\\ I_l\end{bmatrix}=\mathbf{p}\begin{bmatrix}I_{\text{p}}\\ I_{\text{n}}\end{bmatrix}, \quad (4)$$

where the subscripts p and n denote the positive-pole and negative-pole variables, and the subscripts' 0' and 'l' indicate the zero-mode and line-mode variables.

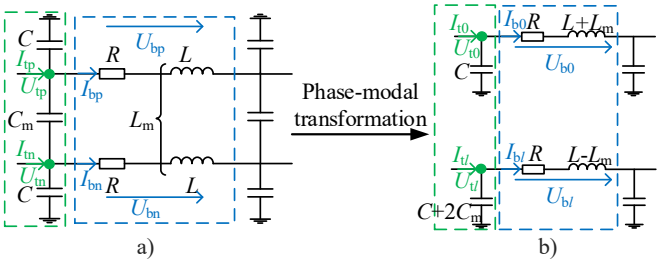

Fig. 5. Decoupling of a π equivalent circuit: (a) π equivalent circuit and (b) decoupled zero- and line-mode circuit.

For simplicity, a π equivalent circuit is taken as an example to explain the decoupling method. Only considering the electromagnetic coupling, the branch impedance matrix is written as:

$$\begin{bmatrix} U_{bp} \\ U_{bn} \end{bmatrix} = \begin{bmatrix} R+sL & sL_m \\ sL_m & R+sL \end{bmatrix} \begin{bmatrix} I_{bp} \\ I_{bn} \end{bmatrix} \tag{5}$$

where R and L are the series resistance and inductance of the signal line, respectively; s is Laplace operator (s=j2πf); and U_{bp}, U_{bn}, I_{bp}, and I_{bn} represent the branch voltages and currents of the positive and negative poles, respectively.

Substituting (4) into (5), the zero-mode and line-mode branch impedance matrix is decoupled, as shown in Fig. 5 (b) and depicted by (6):

$$\begin{aligned} \begin{bmatrix} U_{b0} \\ U_{bl} \end{bmatrix} &= \mathbf{p} \begin{bmatrix} R+sL & sL_m \\ sL_m & R+sL \end{bmatrix} \mathbf{p}^{-1} \begin{bmatrix} I_{b0} \\ I_{bl} \end{bmatrix} \\ &= \begin{bmatrix} R+s(L+L_m) & 0 \\ 0 & R+s(L-L_m) \end{bmatrix} \begin{bmatrix} I_{b0} \\ I_{bl} \end{bmatrix} \end{aligned} \tag{6}$$

where U_{b0}, U_{bl}, $I_{b0,}$ and I_{bl} represent the branch voltages and currents in zero-mode and line-mode, respectively; and R+s(L+L_m) and R+s(L-L_m) are the series impedance of one π equivalent circuit in zero-mode and line-mode, as shown in Fig. 5. Similarly, when only considering the capacitance coupling, the line shunt admittance matrix can also be decoupled:

$$\begin{bmatrix} I_{t0} \\ I_{tl} \end{bmatrix} = \begin{bmatrix} sC & 0 \\ 0 & sC+2sC_m \end{bmatrix} \begin{bmatrix} U_{t0} \\ U_{tl} \end{bmatrix} \tag{7}$$

where U_{t0}, U_{tl}, I_{t0}, and I_{tl} represent the node voltages and currents in zero-mode and line-mode, respectively; sC and sC+2sC_m are the grounding capacitance of one π equivalent circuit in zero-mode and line-mode. According to the decouple zero-mode and line-mode equivalent circuits as shown in Fig. 5 (b), the coupled cascaded π equivalent circuit is transformed into two decoupled circuits as shown in Fig. 6. The number of π circuits is assumed to be k and there are k+1 nodes.

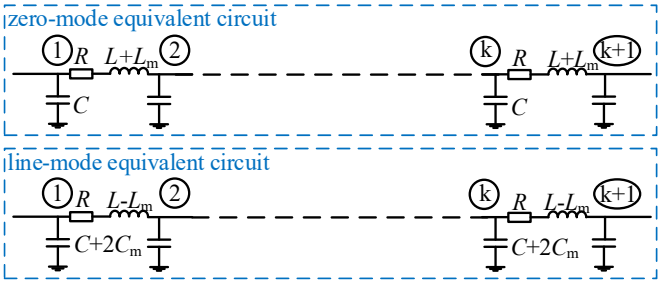

Fig. 6. Line-mode and zero-mode decoupled π equivalent circuits.

From Fig. 6, two k+1 order node admittance matrices in zero-mode and line-modes are both rewritten as (8) due to the same structure:

$$\mathbf{Y}_{(k+1)\times(k+1)} = \begin{bmatrix} Y_{11} & Y_{12} & 0 & \cdots & 0 & 0 \\ Y_{21} & Y_{22} & Y_{23} & \cdots & 0 & 0 \\ 0 & Y_{32} & Y_{33} & \cdots & 0 & 0 \\ \cdots & \cdots & \cdots & \cdots & \cdots & \cdots \\ 0 & 0 & 0 & \cdots & Y_{kk} & Y_{k(k+1)} \\ 0 & 0 & 0 & \cdots & Y_{(k+1)k} & Y_{(k+1)(k+1)} \end{bmatrix} \tag{8}$$

where Y_{pp} (p=1, 2,…, k+1) is the self admittance of node p, Y_{pq} (q=1, 2,…, k+1 and q≠p) represents the mutual admittance between node p and q, and Y_{pq}=Y_{qp}. Taking zero-mode node admittance matrix as an example, Y_{11} is sC+1/(R+sL+sL_m), Y_{12} and Y_{21} are all -1/(R+sL+sL_m), and the other elements in (8) is similarly obtained. As seen in (8), the node x (x=2, 3, …, k) only associates with node (x-1) and (x+1) and thus can be eliminated by using Gaussian Elimination [25], as expressed as:

$$\begin{bmatrix} Y'_{(x-1)(x-1)} & Y'_{(x-1)(x+1)} \\ Y'_{(x+1)(x-1)} & Y'_{(x+1)(x+1)} \end{bmatrix} = \begin{bmatrix} Y_{(x-1)(x-1)} & Y_{(x-1)(x+1)} \\ Y_{(x+1)(x-1)} & Y_{(x+1)(x+1)} \end{bmatrix} - \begin{bmatrix} Y_{(x-1)x} \\ Y_{(x+1)x} \end{bmatrix} Y_{xx}^{-1} \begin{bmatrix} Y_{x(x-1)} & Y_{x(x+1)} \end{bmatrix} \tag{9}$$

Based on (9), the zero-mode k+1 order matrix is simplified as a 2nd order matrix with node 1 and k+1 reserved, as:

$$\begin{bmatrix} I_{10} \\ I_{(k+1)0} \end{bmatrix} = \begin{bmatrix} Y_{011} & Y_{01(k+1)} \\ Y_{0(k+1)1} & Y_{0(k+1)(k+1)} \end{bmatrix} \begin{bmatrix} U_{10} \\ U_{(k+1)0} \end{bmatrix} \tag{10}$$

where Y_{011} and $Y_{0(k+1)(k+1)}$ are the self admittances of node 1 and k+1 in zero-mode; $Y_{01(k+1)}$ and $Y_{0(k+1)1}$ are the mutual admittances between node 1 and k+1; I_{10} is transformed from the positive and negative currents I_{1p} and I_{1n} of node 1; and $I_{(k+1)0}$ is transformed from the positive and negative currents $I_{(k+1)p}$ and $I_{(k+1)n}$ of node k+1.

Similarly, the line-mode node admittance matrix is simplified as:

$$\begin{bmatrix} I_{1l} \\ I_{(k+1)l} \end{bmatrix} = \begin{bmatrix} Y_{l11} & Y_{l1(k+1)} \\ Y_{l(k+1)1} & Y_{l(k+1)(k+1)} \end{bmatrix} \begin{bmatrix} U_{1l} \\ U_{(k+1)l} \end{bmatrix} \tag{11}$$

where Y_{l11} and $Y_{l(k+1)(k+1)}$ are the self admittances of node 1 and k+1 in line-mode; $Y_{l1(k+1)}$ and $Y_{l(k+1)1}$ are the mutual admittances between node 1 and k+1; and I_{1l} and $I_{(k+1)l}$ are transformed from the positive and negative current based on (4).

From (10) and (11), the coupled OHL model is simplified as two-node equivalent models in zero- and line-mode, as shown in Fig. 7.

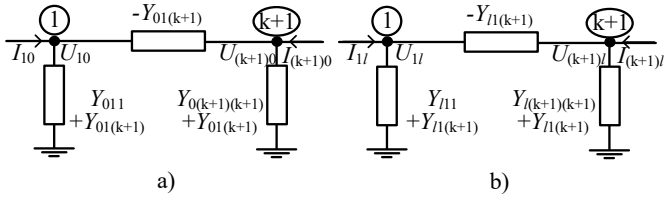

Fig. 7. Two-node equivalent model considering Gaussian Elimination: (a) zero-mode equivalent model and (b) line-mode equivalent model.

B. Frequency-domain characteristics of measured impedance under transient faults

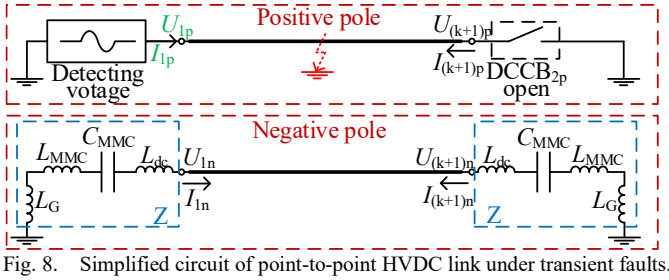

Fig. 8. Simplified circuit of point-to-point HVDC link under transient faults.

After occurrence of positive pole-to-ground faults, the DCCBs at both ends of the faulty line trip. Then the modulated detecting voltage is generated by $DCCB_{1p}$ to identify the type of faults, as previously presented. If the fault is transient, the point-to-point HVDC link in Fig. 3 is simplified as Fig. 8. As seen, $DCCB_{2p}$ remains open, and the converter is represented by the series connection of capacitor C_{MMC} and inductor L_{MMC},

where C_{MMC} and L_{MMC} are equal to $6C_{SM}/N$ and $2L_{arm}/3$, respectively [26]. To describe the frequency-domain characteristics of OHLs, the measured impedance Z_m from the detecting voltage U_{1p} is defined as:

$$Z_m = \frac{U_{1p}}{I_{1p}}. \tag{12}$$

Due to the coupling between the positive and negative poles, the calculation of Z_m is complicated. To solve this problem, the decoupled methods in Section III. *A* is adopted. Based on Fig. 8, the variables at node 1 and k+1 are governed by

$$\begin{cases} U_{1n} = -ZI_{1n} \\ I_{(k+1)p} = 0 \\ U_{(k+1)n} = -ZI_{(k+1)n} \end{cases}, \tag{13}$$

where $Z=s(L_{dc}+L_{MMC}+L_G)+1/sC_{MMC}$ (s=j2πf). Using the phase-mode transformation matrix in (3), (13) is rewritten as:

$$\begin{cases} U_{10} - U_{1l} = -Z(I_{10} - I_{1l}) \\ I_{(k+1)0} + I_{(k+1)l} = 0 \\ U_{(k+1)0} - U_{(k+1)l} = -Z(I_{(k+1)0} - I_{(k+1)l}) \end{cases}. \tag{14}$$

From (10), (11) and eliminating the current quantities, (14) is rewritten as:

$$\begin{cases} Y_{l(k+1)1}U_{1l} + Y_{l(k+1)(k+1)}U_{(k+1)l} + Y_{0(k+1)1}U_{10} + Y_{0(k+1)(k+1)}U_{(k+1)0} = 0 \\ Y_{l(k+1)1}U_{1l} + (Y_{l(k+1)(k+1)} + \frac{1}{Z})U_{(k+1)l} - Y_{0(k+1)1}U_{10} - (Y_{0(k+1)(k+1)} + \frac{1}{Z})U_{(k+1)0} = 0 \\ (Y_{l11} + \frac{1}{Z})U_{1l} + Y_{l1(k+1)}U_{(k+1)l} - (Y_{011} + \frac{1}{Z})U_{10} - Y_{01(k+1)}U_{(k+1)0} = 0 \end{cases} \tag{15}$$

From (15), the coefficients K_1 ($U_{(k+1)l}=K_1U_{1l}$), K_2 ($U_{10}=K_2U_{1l}$), and K_3 ($U_{(k+1)0}=K_3U_{1l}$) are obtained to calculate the impedance Z_m from (10) and (11):

$$Z_m = \frac{U_{1l} + U_{10}}{I_{1l} + I_{10}} = \frac{1 + K_2}{Y_{l11} + K_1 Y_{l1(k+1)} + K_2 Y_{011} + K_3 Y_{01(k+1)}} \tag{16}$$

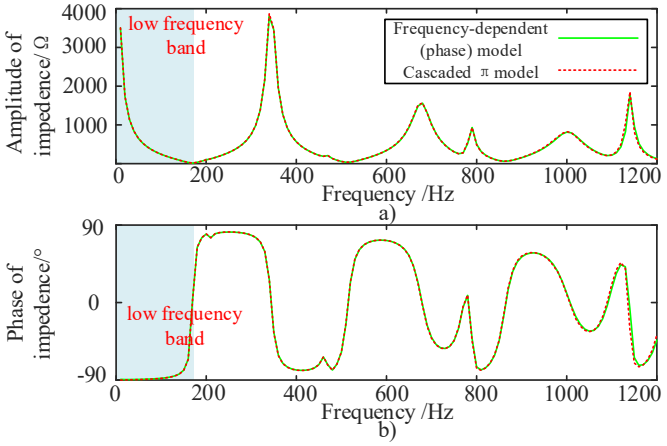

Fig. 9. Impedance comparison between cascaded π model and frequency-dependent (phase) model under transient faults: (a) amplitude-frequency characteristics and (b) phase-frequency characteristics.

When a periodical voltage is applied to the positive line by $DCCB_{1p}$, the measured impedance Z_m with the variation of frequency is calculated from (16). Compared with results obtained from the frequency-dependent model in PSCAD, the calculated Z_m of the cascaded π model is accurate. Thus, the calculation results can represent the characteristics of OHLs, which are capacitive in the low-frequency range (<160 Hz), as shown in Fig. 9.

C. Frequency-domain characteristics of measured impedance under permanent faults

During permanent faults at the positive pole, the simplified system is shown in Fig. 10. Assuming that the fault point is node i and there is also a point at the corresponding position of the negative pole, the OHLs are divided into two parts by the node i and each separate part can only be affected by the other through the node i.

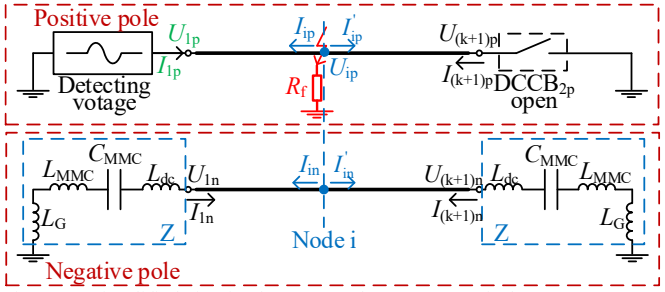

Fig. 10. Simplified circuit of system under permanent faults.

Based on the analysis in Section III. *A*, the two parts of OHLs can be decoupled by the phase-mode transformation matrix and are depicted by (17) and (18) respectively:

$$\begin{cases} \begin{bmatrix} I_{1l} \\ I_{il} \end{bmatrix} = \begin{bmatrix} Y_{l11} & Y_{l1i} \\ Y_{li1} & Y_{lii} \end{bmatrix} \begin{bmatrix} U_{1l} \\ U_{il} \end{bmatrix} \\ \begin{bmatrix} I_{10} \\ I_{i0} \end{bmatrix} = \begin{bmatrix} Y_{011} & Y_{01i} \\ Y_{0i1} & Y_{0ii} \end{bmatrix} \begin{bmatrix} U_{10} \\ U_{i0} \end{bmatrix} \end{cases} \tag{17}$$

$$\begin{cases} \begin{bmatrix} I'_{il} \\ I_{(k+1)l} \end{bmatrix} = \begin{bmatrix} Y'_{lii} & Y_{li(k+1)} \\ Y_{l(k+1)i} & Y_{l(k+1)(k+1)} \end{bmatrix} \begin{bmatrix} U_{il} \\ U_{(k+1)l} \end{bmatrix} \\ \begin{bmatrix} I'_{i0} \\ I_{(k+1)0} \end{bmatrix} = \begin{bmatrix} Y'_{0ii} & Y_{0i(k+1)} \\ Y_{0(k+1)i} & Y_{0(k+1)(k+1)} \end{bmatrix} \begin{bmatrix} U_{i0} \\ U_{(k+1)0} \end{bmatrix} \end{cases} \tag{18}$$

The voltage and current relationship at the fault point i is depicted as:

$$\begin{cases} U_{ip} = -R_f(I_{ip} + I'_{ip}) \\ I_{in} + I'_{in} = 0 \end{cases} \tag{19}$$

According to the phase-mode transformation as depicted by (3), (19) is rewritten as:

$$\begin{cases} U_{i0} + U_{il} = -R_f(I_{i0} + I_{il} + I'_{i0} + I'_{il}) \\ I_{i0} - I_{il} + I'_{i0} - I'_{il} = 0 \end{cases}. \tag{20}$$

Combining (17), (18), (20) with (14), the following equation (21) is obtained to calculate the coefficients K_1, K_2, K_3 in (16). After adjusting the coefficients K_1, K_2, and K_3 in (16), the impedance Z_m with the variation of frequency is calculated and shown in Fig. 11. The impedance under permanent faults is inductive in the low-frequency band (i.e., less than 160 Hz).

As shown in Fig. 9 and Fig. 11, the impedance calculated by the cascaded π equivalent circuit is consistent with the characteristics of the frequency-dependent model under different fault types. Therefore, the features that Z_m remains capacitive during transient faults and inductive during

permanent faults in the low-frequency range (<160 Hz) are utilized in this paper to identify the type of faults, as detailed in the next section.

$$\begin{cases} Y_{l(k+1)i}U_{il}+Y_{l(k+1)(k+1)}U_{(k+1)l}+Y_{0(k+1)i}U_{i0}+Y_{0(k+1)(k+1)}U_{(k+1)0}=0 \\ Y_{l(k+1)i}U_{il}+(Y_{l(k+1)(k+1)}+\dfrac{1}{Z})U_{(k+1)l}-Y_{0(k+1)i}U_{i0} \\ -(Y_{0(k+1)(k+1)}+\dfrac{1}{Z})U_{(k+1)0}=0 \\ Y_{fi1}U_{1l}+(Y_{fii}+Y'_{fii}+\dfrac{1}{R_f})U_{il}+Y_{fi(k+1)}U_{(k+1)l}+Y_{0i1}U_{10} \\ +(Y_{0ii}+Y'_{0ii}+\dfrac{1}{R_f})U_{i0}+Y_{0i(k+1)}U_{(k+1)0}=0 \\ Y_{fi1}U_{1l}+(Y_{fii}+Y'_{fii})U_{il}+Y_{fi(k+1)}U_{(k+1)l}-Y_{0i1}U_{10} \\ -(Y_{0ii}+Y'_{0ii})U_{i0}-Y_{0i(k+1)}U_{(k+1)0}=0 \\ (Y_{l11}+\dfrac{1}{Z})U_{1l}+Y_{l1i}U_{il}-(Y_{011}+\dfrac{1}{Z})U_{10}-Y_{01i}U_{i0}=0 \end{cases} \quad (21)$$

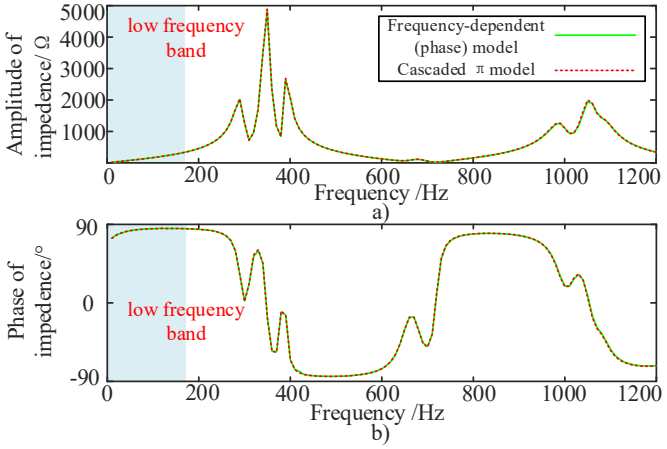

Fig. 11. Impedance comparison between cascaded π model and frequency-dependent (phase) model under permanent faults: (a) amplitude-frequency characteristics and (b) phase-frequency characteristics.

The two-terminal HVDC system is taken as an example for ease of understanding of the frequency-domain characteristics of OHLs. The presented scheme is also applicable to multi-terminal systems, as will be presented in Section V.

IV. Adaptive Reclosing Scheme Based on Phase Characteristics

A. Frequency of the detecting voltage

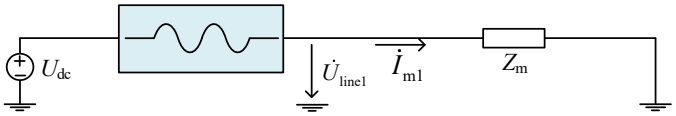

Fig. 12. Equivalent circuit under primary frequency detecting voltage.

As aforementioned, Z_m shows the same capacitive/inductive characteristics as the coupled OHLs in the low-frequency range under transient and permanent faults. Therefore, the fault type can be identified by the different phase characteristics of the measured impedance Z_m, which is calculated by equation (16). In the event of transient faults, the frequency range where the measured impedance Z_m remains capacitive is independent of the fault location and is calculated as 0~160 Hz. Differently, in the occurrence of permanent faults, the frequency at which Z_m remains inductive varies with different fault locations. The calculation results are listed in Table III. As seen, with the variation of fault location, Z_m remains inductive in the frequency range of 0~170 Hz. Therefore, if the frequency of detecting voltage is in the range of 0~160 Hz, the fault type can be accurately discriminated according to the inductive or capacitive characteristic of the measured impedance Z_m. The frequency of the detecting voltage is finally selected as 150 Hz for the tested system to ensure fast and reliable detection. The selected frequency range depends on the system parameters and is variable for different systems but can similarly be determined through the calculation as presented in Section III.

TABLE III
Detecting Frequency Range under Different Faults for Considered System

Fault Location	Fault Type	Detecting Frequency	Feature of Z_m
Head of line	Transient	[0, 160]	Capacitive
	Permanent	[0,1000]	Inductive
Middle of line	Transient	[0, 160]	Capacitive
	Permanent	[0, 340]	Inductive
End of line	Transient	[0, 160]	Capacitive
	Permanent	[0, 170]	Inductive

When identifying fault types, the 150 Hz detecting voltage is applied after 200 ms the fault occurs. Then the voltage and current at the line side of DCCB are measured. The fast Fourier transform (FFT) extracts the primary frequency component of the detecting voltage $\dot{U}_{line1}$ and current $\dot{I}_{m1}$ in Fig. 12 [27]. The impedance is obtained with the primary frequency voltage and current. The DCCB will reclose if the phase of the measured impedance is negative.

B. Flow chart of the proposed scheme

The flow chart of the proposed adaptive reclosing scheme is illustrated in Fig. 13. The scheme is divided into two parts: offline calculation and online identification. In the offline calculation part, the measured impedance under different faults is first calculated using equation (16), where the coefficients are determined by equations (15) or (21). Then, the frequency range that makes the phase positive under permanent faults and negative under transient faults is obtained. Finally, a higher frequency in the range is determined as the detecting frequency with a certain margin. In the online identification part, after the 200 ms extinction of the arc, the detecting voltage is applied by actively controlling the transfer branch of the CFB-DCCB at one terminal of the faulty line, while the CFB-DCCB at the other terminal remains tripped. The phase angle of the measured impedance is then obtained by the primary frequency voltage and current. As the frequency of the detecting voltage is 150 Hz, the phase angle at 20 ms (three cycles) after applying the detecting voltage is used to identify the fault type. If the phase of the measured impedance is positive, i.e. $\arg(\dot{U}_{line1}/\dot{I}_{m1})>0$, the fault is discriminated as permanent. A second threshold of the phase is set to endure the fault resistance up to 2000 Ω. If the phase is larger than θ_{sec}, i.e., -60° in the tested system, the

fault is identified as permanent. Otherwise, the transient faults are detected, and the DCCBs on the faulty lines are reclosed to restore power transmission.

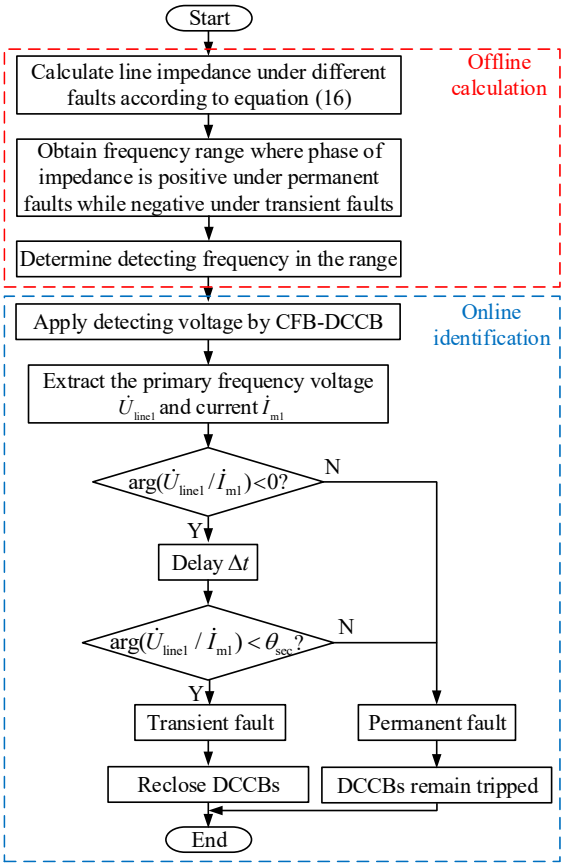

Fig. 13. Flow chart of proposed adaptive reclosing scheme.

V. Simulation Results

The tested two-terminal MMC-HVDC system as shown in Fig. 3 is built in PSCAD/EMTDC, where MMC1 controls the DC voltage of the HVDC link while MMC2 operates on active power control mode. The Thevenin equivalent model is adopted for MMC in the simulations. The OHLs are represented by the frequency-dependent (phase) model. The detailed system parameters are listed in Table I and II. The time instant when applying the detecting voltage is defined as 0. The arc model is simplified as resistance because the arc is usually resistive [28].

A. Verifications under different faults

Based on the analysis in Section II, the detecting voltage is modulated as a square waveform with the frequency of 150 Hz under ideal conditions. Only one SM switches to generate the detecting voltage. Due to the charging process of FBSMs in the transfer branch, the actual detecting voltage and its FFT analysis are shown in Fig. 14. Although the amplitude of the detecting voltage fluctuates, the detecting voltage is dominated by the fundamental frequency component, in addition to the dc component, as shown in Fig. 14 (b). Moreover, the change of the amplitude does not affect the criterion of the proposed scheme and thus the fluctuation can be ignored.

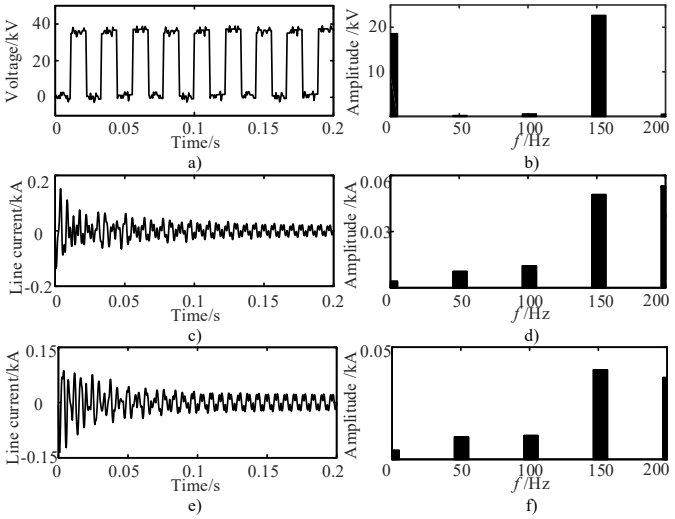

Fig. 14. Waveforms of detecting voltage and line current under different faults: (a) square-wave detecting voltage, (b) FFT analysis of voltage, (c) line current under permanent faults, (d) FFT analysis of current under permanent faults, (e) line current under transient faults and (f) FFT analysis of current under transient faults.

1) Permanent faults

When permanent pole-to-ground faults occur at the middle of the positive OHL, the DCCBs at both terminals of the fault OHLs are open for fault isolation. The detecting voltage is then applied by the DCCB, which leads to a sudden increase of the current at the initial stage due to the permanent fault, as observed in Fig. 14 (c). Then the current stabilizes quickly and is well regulated. During the identification process, the peak of the resultant current is around 0.17 kA, which is in the safe operating range of the equipment. Due to the detecting time of 20 ms, the time window for FFT analysis is selected as 20 ms. Therefore, the components of 50 Hz can be observed in Fig. 14 (d).

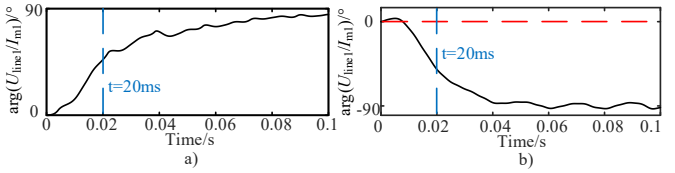

Fig. 15. Primary frequency phase angle: (a) permanent faults and (b) transient faults.

The phase angle $\arg(\dot{U}_{line1}/\dot{I}_{m1})$ at t=20 ms is greater than 0 as shown in Fig. 15 (a), the fault is thus identified as permanent. The detection time of 20 ms is acceptable, as it is much less than the arc extinction time (about 200 ms). The phase angles measured at 20 ms at different locations are listed in Table IV. With the variation of fault location, the proposed scheme can reliably identify the fault as permanent.

TABLE IV
PHASE ANGLE UNDER PERMANENT FAULTS AT DIFFERENT LOCATIONS

Fault location	$\arg(\dot{U}_{line1}/\dot{I}_{m1})$
Head of OHL	54.88°
Middle of OHL	53.33°
End of OHL	37.95°

2) Transient faults

When transient pole-to-ground faults occur, the primary frequency detecting voltage lags the current. Thus, the phase angle $\arg(\dot{U}_{\text{line1}}/\dot{I}_{\text{m1}})$ should be less than 0. The simulation results are shown in Fig. 15 (b). As seen, the phase angle keeps negative after 3 ms, so the angle at 20 ms can be used to identify the fault reliably. Therefore, transient faults can be identified based on the criterion, and a reclosing command will be sent to DCCB. The current caused by detecting voltage is no more than 0.15 kA during this process, as demonstrated in Fig. 14 (e).

Comparing Fig. 14 (d) and (f), the 200 Hz current component is larger than primary frequency under permanent faults while smaller under transient faults. This difference is caused by the resonance of different capacitance and reactance. Therefore, a backup criterion can be established. Comparing with the 150 Hz detecting frequency, if the 200 Hz harmonic component is larger, the fault can be identified as permanent; otherwise, the fault is transient. This will further improve the reliability of the proposed scheme.

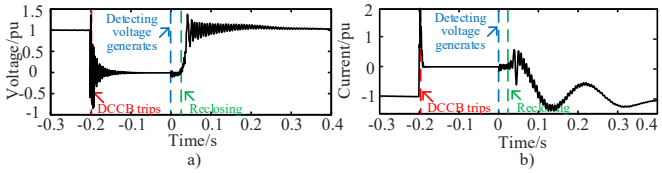

Fig. 16. Waveforms of point-to-point system: (a) DC voltage; (b) DC current

The fault occurs at -0.202 s, and the DCCB trips at -0.2 s. After the 200 ms arc extinguishing interval, the detecting voltage is applied and the DCCB recloses based on the negative phase angle of the measured impedance. The DCCB on the other side of the faulty line recloses when the measured voltage is close to the rated one. The whole system is gradually restored to normal operation at 0.4 s, as shown in Fig. 16.

B. Robustness evaluation

1) Influence of fault resistance

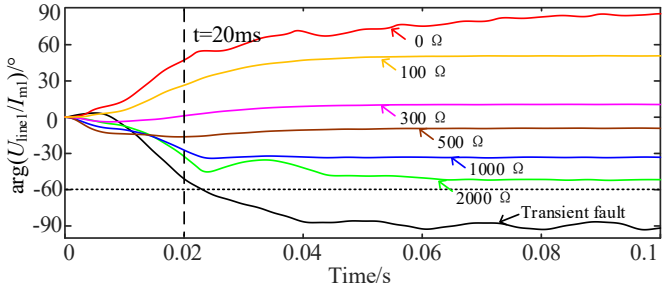

Fig. 17. Primary frequency phase angle with different fault resistances.

To verify the robustness of the proposed scheme to fault resistance, simulations considering different fault resistances up to 2000 Ω are carried out in PSCAD. As can be seen in Fig. 17, the phase angle keeps positive when the fault resistance is smaller than 300 Ω, while negative when the resistance is larger. This problem is solved by adding a second threshold θ_{sec} because the phase angle is not below -60° even under 2000 Ω fault resistance. However, the phase will be around -90° when the fault is transient. Therefore, the θ_{sec} in Fig. 13 is selected as -60° and the time delay Δt is 0.02s to identify the high resistance fault up to 2000 Ω. Hence, the fault resistance has negligible influence on the proposed scheme.

2) Influence of model types

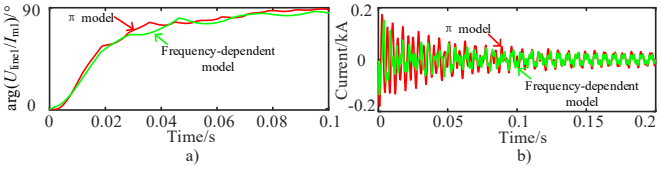

Fig. 18. Comparison of different model types: (a) primary frequency phase angle and (b) lien current.

The frequency-dependent model is the most accurate to represent the transmission lines [9] – [17] and thus is used in all the simulations. The simulations under permanent faults based on the cascaded π model are carried out to verify the robustness of the proposed scheme under different model types. The results in Fig. 18 prove that with different models, the DC currents exhibit different transient characteristics. However, the phase angle of the measured impedance has similar behaviors and remains inductive under permanent faults. Thus, the model types have negligible impacts on the proposed method.

3) Influence of pole-to-pole faults

When the 150 Hz detecting voltage is applied to the pole-to-pole faults, there is a dead zone at the head of the OHL. It is seen from Fig. 19 that the measured phase is positive when the fault occurs at 40 km or longer from the head of line, while negative when the faults in 30 km. This problem can be solved by communication between two terminals of the line, as shown in Table V. When a pole-to-pole fault occurs, the detecting voltage is firstly applied at one terminal. If the phase is positive, the fault is identified as permanent. Otherwise, it stops reclosing and sends a signal. Based on the signal, the DCCB at the other terminal applies the same frequency detecting voltage. If the phase is positive, the fault is permanent. Only when the phases measured at two sides are both negative, then DCCBs reclose.

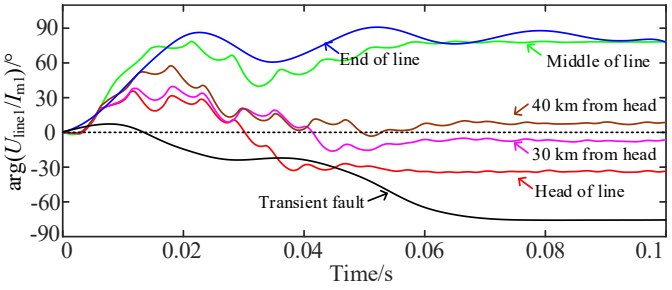

Fig. 19. Primary frequency phase angle under different pole-to-pole faults.

TABLE V
ADAPTIVE RECLOSING SCHEME UNDER POLE-TO-POLE FAULTS

Fault location	Fault type	Phase of measured impedance		Reclosing
		One terminal	Opposite terminal	
Head of line	Permanent	Negative	Positive	×
	Transient	Negative	Negative	√
Middle of line	Permanent	Positive	/	×
	Transient	Negative	Negative	√
End of	Permanent	Positive	/	×

line	Transient	Negative	Negative	√

C. Comparison between proposed method and other schemes

1) Comparison with methods in Group 1 [9] [10].

The methods in group 1 decrease the secondary strike when reclosing on permanent faults. However, it can not elaborate the influence of a failure reclosure and this type of methods couldn't identify the fault type before reclosing. In contrast, the proposed method identifies the fault type before reclosing to ensure the safe recovery of the MMC-HVDC system.

2) Comparison with methods in Group 2 [11] [12] [13].

This group of methods utilizes the line voltage to identify the permanent fault. However, different thresholds of the line voltage need to be set for different systems, and a short time delay is required to avoid the influence of oscillation. For example, the threshold of voltage in [13] is set as 10 kV, and the time delay is 100 ms. The simulations of the methods in Group 2 with the same thresholds are carried out in the tested system. It can be seen in Fig. 20 that the oscillation is severe when the RCB recloses at t=0 s, and DCCB will reclose at t=0.2 s. The recovery time is much longer than other methods. Reference [16] also points out that the reclosing of the RCB will cause a large strike on the IGBTs in the DCCB. In contrast, the proposed method is immune to oscillation, and RCB could act the same way as [16] introduces.

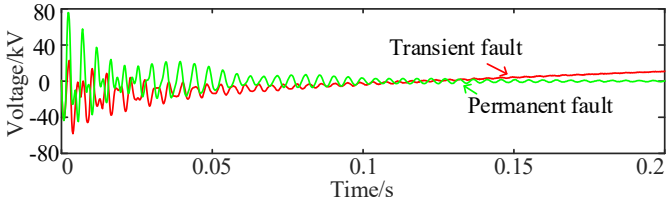

Fig. 20. Simulation results of Group 2 methods in tested system.

The recovery comparison between the proposed method and methods in Group 1 and 2 is shown in Fig. 21. As seen, the methods in Group 1 is the fastest because it recloses directly after 200ms arc-extinguishing interval [9]. The proposed scheme needs tens of milliseconds to identify the fault type before reclosing DCCBs. The voltage-based method is the slowest and to accelerate the system restoration, the protection threshold has to be set differently for different systems [13].

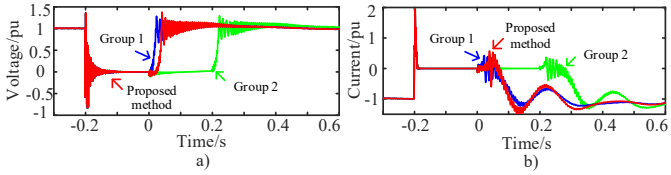

Fig. 21. Comparison diagram between proposed method and Group 1, 2: (a) voltage; (b) current.

3) Comparison with methods in Group 3 [14] [15] [16] [17].

The methods in Group 3 are all based on the characteristics of the traveling wave to identify the fault type and need high sampling frequency to capture the traveling wave and minimize the dead zone of detection. For example, assuming the sampling frequency is f_s, and the traveling wave speed is v (usually 300,000 km/s), the dead zone l is calculated as (22), e.g., the dead zone will be 15 km if the sampling frequency is 10 kHz. Moreover, the traveling wave is sensitive to fault resistance [14].

$$l = \frac{v}{2f_s} \tag{22}$$

The simulation results of the Group 3 methods with different fault resistances and sampling frequencies are shown in Fig. 22. As seen in Fig. 22 (a), when the fault occurs at 2 km from the head of the line, the first reflected surge captured under 50 kHz is not accurate, and the first reflected surge under 10 kHz is missed. Besides, it can be seen in Fig. 22 (b) that the reflected surge under 300 Ω fault resistance is much smaller than that under metallic fault. In contrast, the proposed scheme identifies the fault based on the phase, which requires a low sampling frequency (e.g., 5 kHz) and is robust to fault resistances.

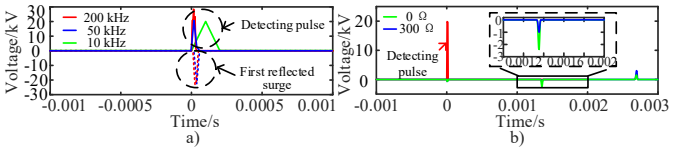

Fig. 22. Simulation results of Group 3 methods in tested system.

The comparison between the proposed method and other works is concluded in Table VI.

TABLE VI
COMPARISON BETWEEN PROPOSED SCHEME AND OTHER ALTERNATIVES

Evaluation index	Group 1 [9] [10]	Group 2 [11] [12] [13]	Group 3 [14] [15] [16] [17]	Proposed scheme
Identify fault type	No	Yes	Yes	Yes
Second strike	Minor	No	No	No
Active control of DCCB	Yes	No	Yes	Yes
High impedance fault	Increased delay	Adaption	Smaller reflected surge	Up to 2000 Ω
Sampling frequency	Low	Low	High	Low
Oscillation	No impact	Delay required	No impact	No impact
Reclose of RCB	No	Yes	No	No
Recovery time	Second min	Max	Min	Second max

D. Verifications for four-terminal MMC-HVDC grid

To demonstrate the validity of the proposed reclosing scheme for multi-terminal HVDC systems, the Zhangbei four-terminal bipolar MMC-HVDC grid rated at ±500 kV [2] is built in PSCAD, as shown in Fig. 23 (a). MMC1 adopts the DC voltage control and other stations operate on active power control mode.

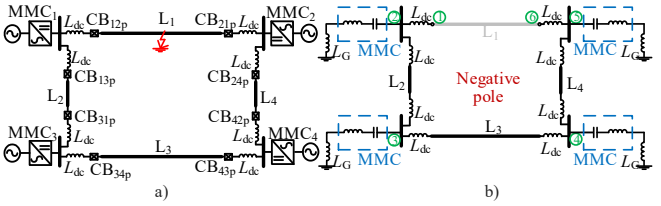

Fig. 23. Zhangbei four-terminal bipolar MMC-HVDC grid: (a) Topology of network and (b) equivalent circuit of negative pole.

At t= -0.2 s, a temporary pole-to-ground fault is applied at

the middle of the positive pole of OHL L_1. The DC voltage of the DC grid drops while the DC current increases, as shown in Fig. 24. The DCCBs CB_{12p} and CB_{21p} are commanded to open for fault isolation. The DC voltage and current of the healthy part recover after fault isolation, while the DC voltage and current of the faulty OHL L_1 remain around zero.

After fault isolation, the equivalent circuit of the negative pole of the four-terminal grid is shown in Fig. 23 (b). To calculate the impedance Z_m of OHL L_1, the impedance of the boundary node 1 and 6 should be obtained first. Because of the isolation of the limiting reactor L_{dc}, the coupling influence between the positive and negative pole of lines L_2, L_3, L_4 can be neglected, and thus they are simplified as the series connection of resistance and reactance. To calculate the boundary impedance, OHL L_1 is removed and a 6-order node admittance matrix is obtained according to Fig. 23 (b). Then, the equivalent impedance of node 1 is derived via the Gaussian Elimination. Due of the network's symmetry, the equivalent impedance of node 6 is the same as node 1, which can be used as a substitution of the impedance Z in (15) and (21). In this way, Z_m of L_1 is obtained and the detecting frequency can be selected as presented in Section IV. After verification, the detecting frequency of 150 Hz is still applicable for MMC-HVDC grid.

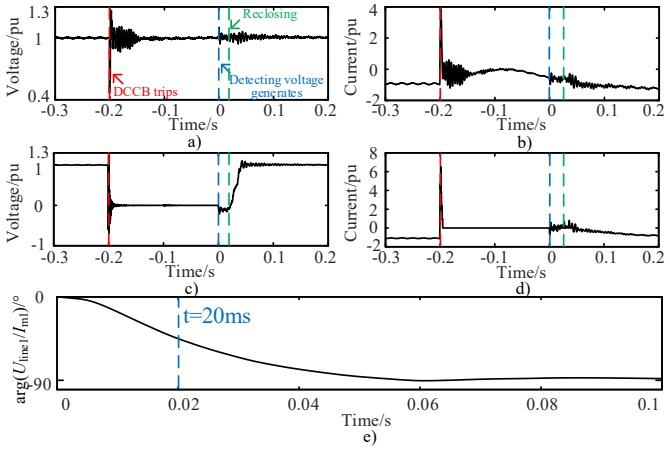

Fig. 24. Voltages and currents under transient fault at OHL L_1: (a) DC voltage of OHL L_2, (b) DC current of OHL L_2, (c) DC voltage of OHL L_1, (d) current of OHL L_1 and (e) primary frequency phase angle.

After arc extinction at t=0 s, the DCCB CB_{12p} is activated and applies the detecting voltage. The resultant current is shown in Fig. 24 and the measured phase angle at t=20 ms is -45.02° as shown in Fig. 24 (e). Thus, the proposed method detects the temporary fault with negligible disturbance on the DC grid during the reclosing process. Then the DCCB CB_{12p} recloses by sequentially bypassing the FBSM capacitors in the transfer branch at t=20 ms, and CB_{21p} recloses according to the increased voltage of OHL. In this way, overvoltage and overcurrent of the DC grid are effectively avoided, as observed in Fig. 24. The system then restores to the pre-fault condition.

VI. Conclusion

An adaptive reclosing scheme based on the phase characteristics is proposed by utilizing the active control of DCCBs and the frequency-domain characteristics of OHLs. This means the method couldn't be used without hybrid DCCB. Based on the phase characteristics of the measured impedance, the detecting frequency is determined, and the criterion of fault type identification can be reliably set. When the phase of the measured impedance is positive, the fault is identified as permanent, and the DCCBs remain tripped. The proposed scheme effectively avoids the risk of failed reclosing and has a limited negative impact on the life of DCCBs. In addition, fault resistances have a negligible influence on the reliability of the proposed scheme, but the non-resistive faults are not considered. The proposed scheme is also applicable to multi-terminal grids without significant effects on the healthy part during the reclosure.

Appendix

Detailed parameters of the Zhangbei four-terminal MMC-HVDC grid are listed in Table AI.

TABLE AI
Parameters of Zhangbei Four-terminal Grid

Parameters	Value
DC reactance L_{dc}	0.15 H
DC line L_1 length	191.6 km
DC line L_2 length	206.8 km
DC line L_3 length	49.5 km
DC line L_4 length	218 km

References

[1] J. Freytes, S. Akkari, P. Rault, M. M. Belhaouane, F. Gruson, F. Colas, and X. Guillaud, "Dynamic analysis of MMC-based MTDC grids: Use of MMC energy to improve voltage behavior," *IEEE Trans. Power Del.*, vol. 34, no. 1, pp. 137–148, Feb. 2019.

[2] M. Kong, X. Pei, H. Pang, J. Yang, X. Dong, Y. Wu, and X. Zhou, "A lifting wavelet-based protection strategy against DC line faults for Zhangbei HVDC Grid in China," in *Proc. 2017 19th Eur. Conf. Power Electron. Appl. (EPE'17 ECCE Europe)*, Warsaw, Poland, Sept. 2017, pp. P.1–P.11.

[3] P. T. Lewis, B. M. Grainger, H. A. Al Hassan, A. Barchowsky, and G. F. Reed, "Fault section identification protection algorithm for modular multilevel converter-based high voltage DC with a hybrid transmission corridor," *IEEE Trans. Ind. Electron.*, vol. 63, no. 9, pp. 5652–5662, Sep. 2016.

[4] L. Tang, and O. Boon-Teck, "Locating and isolating DC faults in multi-terminal DC systems," *IEEE Trans. Power Del.*, vol. 22, no. 3, pp. 1877–1884, Jul. 2007.

[5] D. Jovcic, W. Lin, S. Nguefeu, and H. Saad, "Low-energy protection system for DC grids based on full-bridge MMC converters," *IEEE Trans. Power Del.*, vol. 33, no. 4, pp. 1934–1943, Aug. 2018.

[6] M. Stumpe, P. Ruffing, P. Wagner, and A. Schnettler, "Adaptive single-pole autoreclosing concept with advanced DC fault current control for full-bridge MMC VSC systems," *IEEE Trans. Power Del.*, vol. 33, no. 1, pp. 321–329, Feb. 2018.

[7] T. Wang, G. Song, and K. S. T. Hussain, "Adaptive Single-Pole Auto-Reclosing Scheme for Hybrid MMC-HVDC Systems," *IEEE Trans. Power Del.*, vol. 34, no. 6, pp. 2194-2203, Dec. 2019.

[8] S. Yang, W. Xiang, X. Lu, W. Zuo, and J. Wen, "An Adaptive Reclosing Strategy for MMC-HVDC Systems With Hybrid DC Circuit Breakers," *IEEE Trans. Power Del.*, vol. 35, no. 3, pp. 1111-1123, June 2020.

[9] X. Pei, X., G. Tang, and S. Zhang, "Sequential auto-reclosing strategy for hybrid HVDC breakers in VSC-based DC grids," *J Mod Power Syst Cle*, vol. 7, no. 3, pp. 633–643, May. 2019.

[10] J. Shu, S. Wang, and T. Liu, "A soft reclosing model for hybrid DC circuit breaker in VSC-MTDC system," in *Proc. 2018 IEEE 4th Southern*

Power Electron. Conf. (SPEC), Singapore, Dec. 2018, pp. 1–5.
[11] B. Li, H. Cui, B. Li, W. Wen, and D. Dai, "A permanent fault identification method for single-pole grounding fault of overhead transmission lines in VSC-HVDC grid based on fault line voltage," *Int. J. Electr. Power Energy Syst.*, vol. 117, May. 2020.
[12] J. Liao, N. Zhou, Q. Wang, and N. Wei, "Reclosing Strategy of a Hybrid DC Circuit Breaker on Overhead Lines in Half-Bridge MMC-Based DC Grids Considering Fault Type Discrimination," *IEEE Trans. Power Del.*, to be published. DOI: 10.1109/TPWRD.2021.3064851.
[13] B. Li, J. He, Y. Li, and W. Wen, "A Novel DCCB Reclosing Strategy for the Flexible HVDC Grid," *IEEE Trans. Power Del.*, vol. 35, no. 1, pp. 244-257, Feb. 2020.
[14] G. Song, T. Wang, and K. S. T. Hussain, "DC Line Fault Identification Based on Pulse Injection From Hybrid HVDC Breaker," *IEEE Trans. Power Del.*, vol. 34, no. 1, pp. 271-280, Feb. 2019.
[15] H. Iman-Eini, M. Langwasser, L. Camurca, and M. Liserre, "Modular Hybrid DC Breaker-based Adaptive Auto-Reclosing Method for MMC-HVDC Systems," in *2020 22nd European Conference on Power Electronics and Applications (EPE'20 ECCE Europe)*, 2020, pp. P.1-P.9,
[16] S. Zhang, G. Zou, C. Xu, and W. Sun, "A Reclosing Scheme of Hybrid DC Circuit Breaker for MMC-HVDC Systems," *IEEE J. Emerg. Sel. Top. Power Electron.*, to be published. DOI: 10.1109/JESTPE.2020. 3025598.
[17] J. Mei, R. Ge, P. Zhu, G. Fan, B. Wang, and L. Yan, "An Adaptive Reclosing Scheme for MMC-HVDC Systems Based on Pulse Injection From Parallel Energy Absorption Module," *IEEE Trans. Power Del.*, vol. 36, no. 3, pp. 1809-1818, June 2021.
[18] W. Zhou, X. Wei, S. Zhang, G. Tang, Z. He, J. Zheng, Y.Dan, and C. Gao, "Development and test of a 200 kV full-bridge based hybrid HVDC breaker," in *Proc. 2015 17th Eur. Conf. Power Electron. Appl.*, Geneva, Switzerland, Sept. 2015, pp. 1–7.
[19] J. Sneath, and A. D. Rajapakse, "Fault detection and interruption in an earthed HVDC grid using ROCOV and hybrid DC breakers," *IEEE Trans. Power Del.*, vol. 31, no. 3, pp. 973–981, Jun. 2016.
[20] J. Häfner, and B. Jacobson, "Proactive hybrid HVDC breakers: a key innovation for reliable HVDC grids," in *CIGRE Bologna Symp. - Electr. Power Syst. Future: Integr. Supergrids Microgrids*, Bologna, Italy, 2011, pp. 13-15.
[21] K. Vinothkumar, I. Segerqvist, N. Johannesson, and A. Hassanpoor, "Sequential Auto-Reclosing Method for Hybrid HVDC Breaker in VSC HVDC Links." in *2016 IEEE 2nd Annual Southern Power Electronics Conference* (SPEC), Auckland, New Zealand, Dec. 2016, pp. 1-6.
[22] G. P. Adam, and I. E. Davidson, "Robust and Generic Control of Full-Bridge Modular Multilevel Converter High-Voltage DC Transmission Systems," *IEEE Trans. Power Del.*, vol. 30, no. 6, pp. 2468-2476, Dec. 2015.
[23] M. Ranjbaran, M. M. Tehranchi, S.M.Hamidia, and S.M.H.Khalkhalic, "Effects of square-wave magnetic fields on synchronization of nonlinear spin precession for sensitivity improvement of MX magnetometers," *J. Magn. Magn. Mater.*, vol. 441, no. 1, pp. 718-723, Nov. 2017.
[24] J. R. Marti, "Accurate Modeling of Frequency-dependent Transmission Lines in Electromagnetic Transient Simulations", *IEEE Trans. Power App. Syst.*, vol. 101, no. 1, pp. 147-155, Jan. 1982.
[25] V. Bioglio, M. Grangetto, R. Gaeta, and M. Sereno, "On the fly gaussian elimination for LT codes," *IEEE Commun. Lett.*, vol. 13, no. 12, pp. 953-955, Dec. 2009.
[26] W. Xiang, S. Yang, L. Xu, J. Zhang, W. Lin, and J. Wen, "A Transient Voltage-Based DC Fault Line Protection Scheme for MMC-Based DC Grid Embedding DC Breakers," *IEEE Trans. Power Del.*, vol. 34, no. 1, pp. 334-345, Feb. 2019.
[27] F. J. Harris, "On the use of windows for harmonic analysis with the discrete Fourier transform," *Proc. IEEE*, vol. 66, no. 1, pp. 51-83, Jan. 1978.
[28] T. Gammon, W. Lee, Z. Zhang, and B. C. Johnson, "A Review of Commonly Used DC Arc Models," *IEEE Trans. Ind. Appl.*, vol. 51, no. 2, pp. 1398-1407, April 2015.

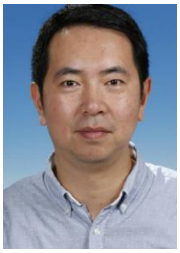

Tao Zheng (M'13) was born in Shandong, China, in 1975. He received the Ph.D. degree in power systems and automation from North China Electric Power University (NCEPU), Beijing, China, in 2005. He is currently a Professor with the School of Electrical and Electronic Engineering, NCEPU. His research interests are focused in the area of power system protection.

Wenxuan Lv was born in Jiangsu, China, in 1996. He received a bachelor's degree in electrical engineering from North China Electric Power University, Beijing, in 2019. He is currently pursuing the Ph.D. degree in electrical engineering with North China Electric Power University. His research interest is flexible DC system protection and control.

Rui Li (M'18) received the M.S. and Ph.D degrees in electrical engineering from Harbin Institute of Technology, Harbin, China, in 2008 and 2013, respectively. He is a researcher with University of Strathclyde in Glasgow, UK, since 2013.
His research interests include HVDC transmision systems, grid integration of renewable power, power electronic converters, and energy conversion.